Available online at www.sciencedirect.com
SCIENCE DIRECT®
International Journal of Heat and Mass Transfer 48 (2005) 2856–2867
International Journal of HEAT and MASS TRANSFER
www.elsevier.com/locate/ijhmt

Mechanically aspirated radiation shields: A CFD and neural network design analysis

R.L. Mahajan [a,*], B.M. Fichera [a], T.W. Horst [b]

[a] Department of Mechanical Engineering, University of Colorado, Boulder, CO 80309, United States
[b] UCAR, Boulder, CO 80309, United States

Received 2 December 2004; received in revised form 31 January 2005
Available online 14 April 2005

Abstract

Accurate air temperature measurements made by surface meteorological stations are demanded by climate research programs for various uses. Heating of the temperature sensor due to coupling with the environment can lead to significant errors. Therefore, accurate in situ temperature measurements require shielding the sensor from exposure to direct and reflected solar radiation, while also allowing the sensor to be brought into contact with atmospheric air at the ambient temperature. The difficulty in designing a radiation shield for such a temperature sensor lies in satisfying these two conditions simultaneously. In this paper, we perform a computational fluid dynamics analysis of mechanically aspirated radiation shields (MARS) to study the effect of geometry, wind speed, and interplay of multiple heat transfer processes. Finally, an artificial neural network model is developed to learn the relationship between the temperature error and specified input variables. The model is then used to perform a sensitivity analysis and design optimization.

Keywords: Artificial neural networks; CFD; Mechanically aspirated radiation shields

1. Introduction

Air temperature measurements made by surface meteorological stations have many uses. They lead to the mapping of temperature profiles, which are used as a means of estimating surface heat fluxes. Their use on land is common in mesoscale networks such as the National Center for Atmospheric Research (NCAR) Portable Automated Mesonet [1,2] and the Oklahoma Mesonet [3]. Accurate in situ temperature measurements require shielding the sensor from exposure to direct and reflected solar radiation, as well as thermal radiation emitted by the ground and sky. The shield design must also allow the sensor to be brought into contact with atmospheric air at the ambient temperature. This complicates the design of an effective radiation shield. Likewise, sensors that measure relative humidity must also be shielded if the humidity is to be interpreted in terms of the measured air temperature.

The two main types of solar radiation shields are: (i) naturally ventilated and (ii) mechanically aspirated. Many of the designs and investigations that have appeared in literature concern naturally ventilated multiplate radiation shields [4–6]. However, errors in excess of 1 °C are not uncommon in naturally ventilated shields for wind speeds less than 1–2 m/s [4,5]. This is not acceptable in certain applications where temperature

* Corresponding author. Tel.: +1 303 492 7750; fax: +1 303 492 3498.
E-mail address: mahajan@spot.colorado.edu (R.L. Mahajan).

0017-9310/$ - see front matter © 2005 Elsevier Ltd. All rights reserved.
doi:10.1016/j.ijheatmasstransfer.2005.01.026

Nomenclature

a_{10}, a_p	solar absorptivity (short-wave emissivity) of the outer shield and probe, respectively
A	outer surface area of a shield component
A_g	ground albedo
$\bar{I}_0$	solar radiation vector
L	outer shield length
$\hat{n}$	surface unit normal vector
r_i, r_j	radius of shield inlet and the probe base, respectively
R	inlet radius of curvature
R^2	correlation coefficient
$T_{L+\Delta L}$, T_L	temperature error at length $L+\Delta L$ and L, respectively
$T_{R+\Delta R}$, T_R	temperature error at inlet radius of curvature $R+\Delta R$ and R, respectively
$T_{W+\Delta W}$, T_W	temperature error at wind speed $W+\Delta W$ and W, respectively
vf_g, vf_s	view factor from ground to vertical outer shield and from shield inlet to probe base, respectively
V	volume of shield component
W	wind speed
XS	distance from shield inlet to base of temperature probe

Greek symbols

ΔL	small change in shield length
ΔR	small change in inlet radius of curvature
ΔW	small change in wind speed
$\bar{\varepsilon}_{REL}$	percentage relative error
$\bar{\varepsilon}_{MSE}$	average mean squared error (MSE)
θ	solar zenith angle, measured in radians from vertical

Subscripts

10	outer surface of outer shield
g	ground
p	probe base
s	shield inlet
i	shield inlet radius
j	probe base radius
L	outer shield length
R	inlet radius of curvature
W	wind speed

errors on the order of a few tenths of a degree can be important. Mechanically aspirated radiation shields (MARS) are therefore often suggested as the preferred shield type. However, no in-depth analysis of the performance of mechanically aspirated shields exists in the literature. Therefore, a systematic design study of MARS is needed.

The NCAR Integrated Surface Flux Facility is composed of a number of remote meteorological stations powered by solar-charged batteries. Due to the long duration of use and remoteness of some sites, these stations have very narrow power constraints. Therefore, a low-power aspirator is required to support the measurement of more accurate temperatures [4]. The low power requirement is often the reason for using naturally ventilated shields. In order to use a mechanically aspirated shield and still satisfy the power requirements, a low power fan must be used. As a result, an effective low power shield can be obtained only by carefully optimizing the design.

The performance of a solar radiation shield depends on the interplay of multiple heat transfer processes between the shield and the environment as well as the different components of the shield. Optimization of a radiation shield design requires a model that integrates all of these effects. Utilizing computational fluid dynamics (CFD), shield performance, as measured by temperature error, can be assessed and characterized easily.

In recent years, artificial neural networks (ANNs) have emerged as an efficient tool for providing quick, almost real-time analysis, as well as for optimization of nonlinear problems with several inputs and outputs. In particular, Mahajan and Wang [7], Kelkar et al. [8], and Calmidi and Mahajan [9] have shown that an ANN model trained on numerical data obtained through simulations of physics-based models can be very efficient in obtaining an optimum design for a specific process.

In this paper, we combine the power of CFD and ANNs to develop an optimum radiation shield design. The radiation shield design is discussed in the next section. The CFD and heat transfer models are developed in Section 3 and several computer simulations are presented for a range of input parameters. A discussion of an artificial neural network trained and verified with the CFD data and used for sensitivity analysis and optimization is included in Section 4. The last section summarizes the results.

2. Shield design

There exists little guidance in the literature concerning the design of mechanically aspirated radiation shields. The NCAR shield used in the current investigation places the temperature sensor on the axis of two

vertical, metal concentric cylinders, with the sensor recessed some distance from the inlet. Ambient air is drawn past the sensor through the use of a low power axial fan placed in a horizontal exhaust duct attached to the vertical concentric cylinders, see Fig. 1 for a cross-sectional view of the radiation shield. The vertical shields have a length of 27.31 cm and the diameters of the outer shield and inner shields are 3.49 cm and 2.54 cm, respectively. The sensor is encased in the Vaisala HUMITTER® temperature probe on the vertical centerline.

The main design variables affecting the performance of MARS are the inlet shape of the shield, the length of the vertical shields, and the sensor location within the shield geometry. There are several environmental variables affecting shield performance. These include wind speed, solar radiation intensity, solar zenith angle, ground albedo and ground surface temperature. Assuming daytime, clear sky conditions, a constant zenith angle and surface properties, the wind speed is expected to have a large effect on shield performance.

In the presence of high wind speeds, there is a region of separation and recirculating flow near the inlet. The reason for placing the sensor away from the inlet is to ensure that the flow be fully developed and that the sensor be not in the middle of recirculating flow. However, since the aspirated air temperature increases with axial distance from the inlet due to heat gain from the shield, an optimum location for sensor placement may exist that strikes a balance between the two effects.

Three different shield length/sensor placement combinations were tried. The first geometry consists of a 27.31 cm long outer shield with the tip of the 7.62 cm long probe recessed 19.69 cm from the inlet of the inner shield. The medium length shield has the probe recessed 5.56 cm from the inlet of the inner shield (outer shield length of 13.69 cm) and the shortest design has the temperature probe tip even with the inlet of the inner shield (outer shield length of 8.13 cm).

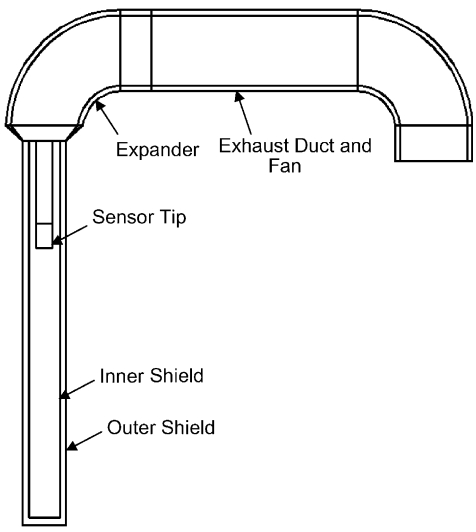

Fig. 1. Radiation shield geometry.

The other geometry modification studied was the shape of the inlet section that was demonstrated in an NCAR field project in Oklahoma in 1998 to influence the shield performance. Temperature error in the NCAR aspirated shield with a straight circular inlet was seen to increase at higher wind speeds. This was attributed to a dramatic drop in the flow rate through the shield at high wind speeds. The addition of bell-shaped flared inlets was seen to improve aspiration rate at higher wind speeds in wind tunnel experiments. This motivated our inclusion of flared bell-shaped inlets of constant radii of curvature of 0.43 cm, 0.84 cm, and 1.27 cm in addition to the straight inlet in our study.

The heat balance of the shield, in addition to convective cooling, is also governed by shield material properties that control radiative heat transfer. Fuchs and Tanner [10] studied the effect of a number of shield coatings with selective absorption characteristics for solar and thermal radiation. They showed that shield coatings with selective absorptivities can be chosen to minimize temperature error. The shield materials should have a low solar emissivity to thermal emissivity ratio. They found the temperature error was reduced most for the surface coatings of aluminized Mylar, white paints, white porcelain, and aluminum foil with clear finishes. The design employed in our investigation uses brass shields coated with white paint. The exhaust duct is made of white PVC piping and the bell-shaped inlets are made of white Delrin plastic.

Meteorological stations employing shielded temperature sensors are often powered by solar energy. The solar power system comprises a solar panel, a regulator, a battery, and an enclosure. Power consumption of these remote stations can be set as low as 1.5 W [3]. In one such network, the Oklahoma mesonet, the data logger with the modem, transceiver, and a full suite of sensors consumes just under 1 W [3]. Thus, the fan should consume as little power as possible. The fan used in the current design is a Micronel axial fan model V581L. It is a small DC current fan (6/12 V) with a power requirement of only 0.42 W.

3. Numerical simulations

3.1. Flow simulations

In order to assess the performance of different mechanically aspirated shield designs, numerical simulations were run with the FLUENT computational fluid dynamics (CFD) package. This package provides an

attractive method for examining the flow through the shields subject to various design modifications. Additionally, numerical simulations provide more detailed information than the wind tunnel about flow characteristics inside the shield such as separation regions and recirculating flow patterns. In addition, the FLUENT model with a capability to include heat transfer model, also allows for the temperature error to be obtained for a wide range of cases.

Meshed geometry files covering the range of shield designs studied were created and run in FLUENT. Unstructured meshes were chosen because of the ease of grid generation. Local grid refinements could be made based on velocity gradients. The meshes were refined until grid independent solutions were established. The flow simulations were performed using air as the working fluid at standard atmospheric temperature and pressure. All simulations were 3D simulations with the y-direction being the vertical direction and the horizontal exhaust duct extending in the x-direction. Ambient wind was simulated by specifying a constant, uniform, horizontal velocity inlet boundary on a large, meshed rectangular domain surrounding the radiation shield geometry. The extent of this domain was selected to ensure that far away from the shield, the ambient flow field was not affected by the presence of the shield. To this end, the computational domain was enlarged in steps until horizontal velocity condition was achieved.

To validate the flow simulations, wind tunnel experiments were conducted at NCAR to measure the flow speed inside the shield as a function of external wind speed. Four different inlet geometries (3 flared inlets and 1 straight inlet) were used on the longest shield design (27.31 cm shields). Airflow inside the shield was measured on the vertical shield axis using a Thermo Systems, Inc., 1D hot film air velocity transducer. The sensing head was recessed approximately 19.69 cm from the inlet, corresponding to the tip of the temperature probe. Results from the wind tunnel experiments and CFD simulations can be seen in Fig. 2. For still wind, the aspiration velocity at the hot wire probe is ~3.25 m/s and is entirely due to the fan. At low wind speeds, the aspiration velocity increases with increase in the wind speed. However, beyond some value of the wind speed the aspiration velocity starts decreasing until at some value of wind speed, flow reversal takes place. We note that the simulations correlate well with the wind tunnel data, with the maximum difference in aspiration rate being less than 0.2 m/s.

Representative flow field simulations are shown in Fig. 3 which shows the velocity vector plots for the medium length shield for wind speed of 0.1 m/s and 5.0 m/s for the straight inlet (Fig. 3(a) and (b)) and of 5 m/s for the large bell-shaped inlet (Fig. 3(c)). The flow recirculation is clearly seen for the straight inlet at 5 m/s wind. This effect is much less pronounced for the large

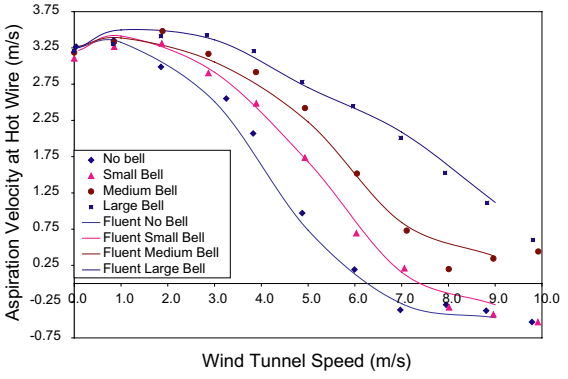

Fig. 2. Flow rate in the aspirated shield at a recessed distance of 19.69 cm.

bell inlet design. Other shields of different lengths showed different thresholds of wind speed for the recirculating flows. For example, for the small bell-shaped inlet, flow reversal is avoided for wind speeds <7 m/s. On the other hand, for the two largest bell-shaped inlets, no flow reversal was observed. The key point is that altering the inlet geometry of the shield can significantly influence the flow region in the inlet region and hence, the flow past the temperature probe.

3.2. Heat transfer model

Shield performance with respect to temperature error is evaluated by modeling the heating due to solar and thermal radiation and solving the energy equation. The external solar heat flux is modeled in FLUENT as a heat generation rate within the meshed solid wall of the outer shield. Converting the incident solar heat flux into a heat source in the shield is done by specifying the heat generation rate as

$$\text{Source} = a_{10}[A/V[\overline{I}_0 \cdot \hat{n} + I_0 \mathrm{vf}_g A_g \cos(\theta)]] \ (\mathrm{W/m^3}) \quad (1)$$

The first term is the direct solar radiation and uses the dot product of the solar radiation vector and the unit normal vector of the outer surface of the shield. The second term is the reflected radiation from the ground. The above equation can be applied to each component simply by using a different A/V for each volume element.

Since the exhaust duct components are all made of PVC plastic, thermal resistance in the exhaust duct is higher compared to that in the brass shields. Also, since the exhaust duct elements are all downstream of the brass shield with respect to internal flow, heating of the exhaust duct does not affect the temperature of the air inside the brass shield where the sensor is located. Because of these two simplifying assumptions, Eq. (1) is only applied to the outer brass shield and the expansion section of the exhaust duct, see Fig. 1, without any significant loss in accuracy. Additionally, Eq. (1) is applied

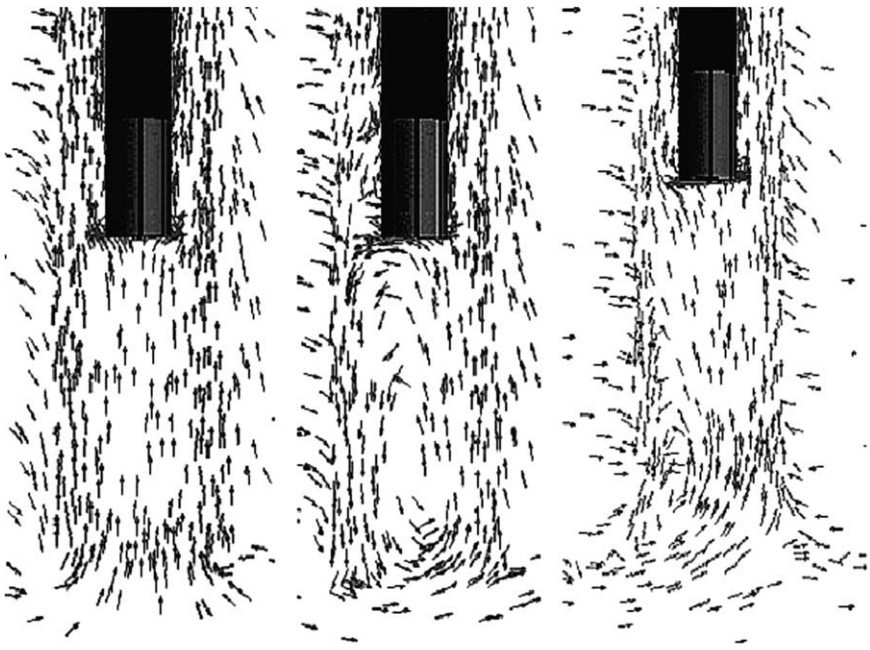

Fig. 3. Velocity vectors for: (a) straight inlet and 0.1 m/s wind speed; (b) straight inlet and 5 m/s wind speed; (c) large bell-shaped inlet and 5 m/s wind speed.

to the bell volumes for the flared inlets as well since they are upstream of the temperature sensor.

A second heat generation rate equation was used to account for the reflected solar radiation from the ground entering the inlet of the shield geometry. This heat generation rate is specified on the base of the temperature probe surrounding the sensor as

$$\text{Source} = (A/V)(\text{vf}_\text{s})(a_\text{p})(A_\text{g})(I_0)\cos(\theta)\ \ (\text{W/m}^3) \tag{2}$$

The view factor was obtained from [11] as

$$\begin{aligned} R_i &= r_i/\text{XS}, \quad R_j = r_j/\text{XS} \\ S &= 1 + \frac{1+R_j^2}{R_i^2} \\ \text{vf}_\text{s} &= \frac{1}{2}\{S - [S^2 - 4(r_j/r_i)^2]^{\frac{1}{2}}\} \end{aligned} \tag{3}$$

The outer shield has a solid mesh for purposes of specifying the heat generation in Eqs. (1) and (2) while the inner shield is modeled as a thin wall. A wall thickness (0.11 cm) is specified for the inner shield and FLUENT solves a 1D planar conduction equation in this wall.

3.3. Design of experiments

To investigate the impact of each variable on the resulting temperature error, a statistical design of experiments was used to set up an experimental matrix. Since the FLUENT solutions are used as input to the neural network model to train, test, and validate it, enough simulation runs were needed in order to allow the neural network to correctly model the physics of the problem. The three main input variables along with the different levels for each are listed in Table 1.

In order to keep the number of FLUENT runs manageable, and due to CPU time and memory constraints, six discrete wind speeds between 0 and 10 m/s were chosen. The inlet geometry is a continuous variable when measured in terms of the radius of curvature of the bell-shaped inlets. Shield length is also a continuous variable. The four specific inlet designs listed in Table 1 were modeled in FLUENT because they were previously tested in the wind tunnel and used for validation of the

Table 1
Input variables and their levels

Input variable	Range
Inlet geometry	Straight
	0.43 cm flare radius
	0.84 cm flare radius
	1.27 cm flare radius
Length of shield/recessed distance	27.31 cm/19.69 cm
	13.69 cm/5.56 cm
	8.13 cm/0.51 cm/0.51 cm
Wind speed	0.1, 1, 3, 5, 7, and 9 m/s

flow model. The shield length variable was given three levels. The long shield is the shield length currently used in field projects. The medium length shield was built at NCAR for testing purposes and the short length shield allows for the other extreme case to be modeled. The range and levels for each variable are based on past results and engineering judgment.

With six wind speeds, four inlet designs, and three lengths, a total of $6 \times 4 \times 3 = 72$ simulations were run in FLUENT. These 72 runs account for all possible combinations of each variable level listed in Table 1. The FLUENT experiments were run on a Sun Ultrasparc machine at NCAR. For each simulation, the temperature of the sensor surface minus the ambient air temperature entering the modeled domain was reported as the temperature error subject to the environmental conditions. These 72 FLUENT simulations were then used as input data to develop a neural network model on the CU-ANN© software at the University of Colorado.

3.4. FLUENT results

The 72 runs covering the range of variables listed in Table 1 were run in FLUENT. The errors for long, medium and short shields for different wind speeds and inlet section design are listed in Tables 2–4. First consider the longest shield with the straight inlet. With increasing wind speed and decreased aspiration, the temperature error in the shield rises considerably as observed in past field projects. With an increase in flare radius, the flow field indicated a decrease in recirculation resulting in increased aspiration rate and hence reduced temperature error. With the 1.27 cm flare radius inlet, the maximum temperature error seen was 0.179 °C at a wind speed of 7 m/s compared to an error of 0.990 °C at the same wind speed for the straight inlet. All shield designs perform similarly at low wind speeds where aspiration rate is the same for each shield. These results can be seen in Fig. 4.

For the medium length shield, the same trends are observed. However, the temperature error for all the inlets is significantly lower for the corresponding long shield. Note the change in the range of the y-axis. In the medium length shield, the maximum temperature error for the straight inlet is 0.230 °C at a wind speed of 9 m/s and the largest error seen for the large bell-shaped inlet is 0.056 °C at a wind speed of 7 m/s. Thus, compared to the longest shield, placing the sensor closer to the inlet and shortening the length of the shield reduces the temperature error by more than a factor of 4 for the straight inlet and by more than a factor of 3 for the large bell-shaped inlet. Again, the flared inlets show reduced error at high wind speeds due to higher aspiration rates. The results for the medium length shield can be seen in Fig. 5.

Table 2
Errors for the long shield

Inlet geometry	Wind speed (m/s)	Temperature error (°C)	Aspiration rate (m/s)
Straight	0.1	0.078	3.261
Straight	1	0.038	3.326
Straight	3	0.277	2.509
Straight	5	0.491	0.735
Straight	7	0.990	−0.278
Straight	9	1.074	−0.470
Small bell	0.1	0.072	3.216
Small bell	1	0.043	3.414
Small bell	3	0.147	2.914
Small bell	5	0.276	1.677
Small bell	7	1.021	0.156
Small bell	9	1.095	−0.293
Medium bell	0.1	0.081	3.273
Medium bell	1	0.042	3.387
Medium bell	3	0.108	3.055
Medium bell	5	0.154	2.328
Medium bell	7	0.276	0.803
Medium bell	9	0.259	0.324
Large bell	0.1	0.076	3.254
Large bell	1	0.035	3.498
Large bell	3	0.064	3.361
Large bell	5	0.104	2.703
Large bell	7	0.179	2.088
Large bell	9	0.083	1.120

The temperature errors for the shortest shield length, with the temperature probe even with the inlet of the inner shield, are of the same order as those for the medium length shield. The maximum error for the straight inlet and large bell inlet are 0.271 °C and 0.130 °C, respectively. The interesting result is that the short shield temperature errors are higher than those for the medium length shield for all wind speeds. One difference seen between the short shield results and the other two shield lengths is that the temperature error reaches a maximum somewhere between wind speeds of 5 and 7 m/s and begins to decrease for all inlet geometries. This different trend is due to the different flow field and the concomitant heat transfer characteristics experienced by the temperature probe. For the shortest shield, the temperature probe is located in the inlet region where recirculating flow is observed in FLUENT. For the two longer shield designs, the probe is farther downstream where the flow is more developed and uniform throughout the shield.

In addition to the differences in the convective flow fields due to the length and shape of the inlet section, the radiation heat exchange between the heat shield and the surroundings plays a role in determining the temperature error. First we note that the air temperature inside the shield increases with axial distance for all external heating conditions and aspiration rates and

Table 3
Errors for the medium length shield

Inlet geometry	Wind speed (m/s)	Temperature error (°C)	Aspiration rate (m/s)
Straight	0.1	0.028	3.172
Straight	1	0.011	3.381
Straight	3	0.068	2.422
Straight	5	0.194	0.715
Straight	7	0.230	−0.309
Straight	9	0.230	−0.372
Small bell	0.1	0.026	3.136
Small bell	1	0.011	3.269
Small bell	3	0.050	2.984
Small bell	5	0.118	1.593
Small bell	7	0.221	0.302
Small bell	9	0.216	−0.256
Medium bell	0.1	0.025	3.093
Medium bell	1	0.009	3.279
Medium bell	3	0.027	3.296
Medium bell	5	0.076	2.470
Medium bell	7	0.118	0.865
Medium bell	9	0.080	0.419
Large bell	0.1	0.029	3.200
Large bell	1	0.009	3.481
Large bell	3	0.006	3.679
Large bell	5	0.050	2.741
Large bell	7	0.056	2.150
Large bell	9	0.051	1.321

Table 4
Temperature errors for the short shield

Inlet geometry	Wind speed (m/s)	Temperature error (°C)	Aspiration rate (m/s)
Straight	0.1	0.050	N/A
Straight	1	0.042	N/A
Straight	3	0.117	N/A
Straight	5	0.271	N/A
Straight	7	0.270	N/A
Straight	9	0.201	N/A
Small bell	0.1	0.049	N/A
Small bell	1	0.042	N/A
Small bell	3	0.095	N/A
Small bell	5	0.241	N/A
Small bell	7	0.269	N/A
Small bell	9	0.204	N/A
Medium bell	0.1	0.054	N/A
Medium bell	1	0.042	N/A
Medium bell	3	0.086	N/A
Medium bell	5	0.147	N/A
Medium bell	7	0.148	N/A
Medium bell	9	0.132	N/A
Large bell	0.1	0.059	N/A
Large bell	1	0.041	N/A
Large bell	3	0.059	N/A
Large bell	5	0.098	N/A
Large bell	7	0.130	N/A
Large bell	9	0.124	N/A

the total amount of heat absorbed is proportional to shield length. Placing the sensor deep within the shield exposes it to higher temperatures since the amount of heat absorbed by the shield and transmitted to the aspirated air is proportional to shield length. The suggestion is that the longer the shield, the larger the error. For example, the average outer shield temperature for 0.1 m/s wind speed was 2.3 °C, 1.4 °C, and 1.2 °C for the long, medium length, and short shields, respectively. However, the results for the medium length and short shields show that there is a penalty for placing the sensor too close to the inlet. The amount of long wave radiation reaching the sensor from the ground increases as it is placed closer to the inlet. To test this, the FLUENT model was first run without any long wave radiation exchange between the ground and the shield geometry. That FLUENT model predicted the shortest shield to have temperature errors very similar to the medium length shield. When long wave emission from the ground was added to the FLUENT model, the temperature errors for the shortest shield length increased significantly while the temperature errors for the long and medium length shields were relatively unchanged at low wind speeds. The long and medium length shields did show measurable increases at high wind speeds with long wave radiation from the ground added to the model. (All data listed in the figures and tables were obtained with the FLUENT model including long wave ground loading.)

In summary, over the entire range of shield designs, the temperature error is a minimum at low wind speeds where the aspiration rates are a maximum. At high wind speeds, the temperature error increases for all shield lengths and inlet designs due to decreased aspiration. In the range of inlet designs considered, the temperature error decreases with an increase in the flare radius. The

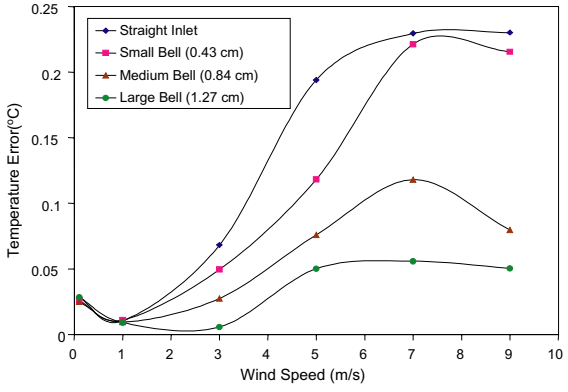

Fig. 4. Temperature error for the longest length shield.

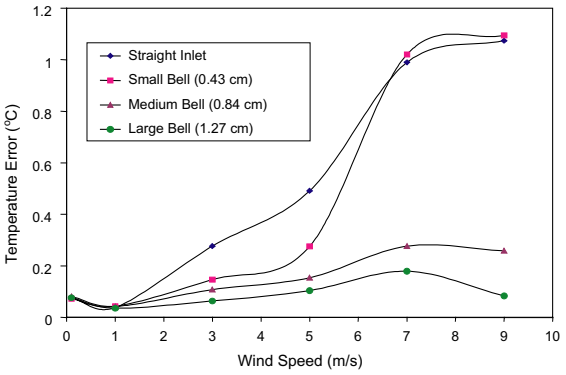

Fig. 5. Temperature errors for the medium length shield.

length of the shield impacts the radiative heat exchange and the temperature error in a complex manner.

We next compare our computer solutions with results from past field experiments. The experimental data are from a 1998 NCAR field project in Oklahoma (OASIS98). This project studied vertical temperature profiles by placing sensors at heights of 1.5, 4.5, and 9 m. The data collected on several afternoons with wind speeds in the range of 4–5 m/s at the 1.5 m height and in the 5–7 m/s range at the 9 m sensor height were selected to compare with the corresponding FLUENT predictions. The OASIS98 data are reported as the difference between the temperature recorded with the Gill multiplate shield and the temperature recorded with the NCAR aspirated shield. For wind speeds between those studied with FLUENT, the FLUENT data were interpolated from Fig. 4. The correlation between the FLUENT model and the OASIS98 data was found to be excellent. The relative errors of the FLUENT model range from 0.60% to 10.26%.

The results of the OASIS98 project also suggest that the mechanically aspirated shields perform well for low wind speeds and perform poorly at higher wind speeds. The FLUENT results suggest that this is due to the dramatically decreased aspiration rate for the straight inlet at high wind speeds.

We note that the FLUENT model calculates temperature errors due solely to poor coupling with the environment. It does not take into account inherent errors of the sensor itself or any heating due to the motor of the fan. The temperature sensor can be calibrated to within 0.01–0.02 °C. Additionally, heating of the aspirated air due to the motor of the fan is expected to be minimal since the fan is downstream of the temperature sensor and probe geometry.

The main uncertainty in determination of the temperature error with FLUENT arises from the inherent variance in the CFD model. Several FLUENT simulations were repeated and the average variation in the FLUENT model was found to be approximately 0.02 °C. The main uncertainty in experimental determination of temperature error in the field, other than sensor calibration mentioned above, is the fact that the reference temperature recorded with the naturally ventilated shield is subtracted from the temperature recorded by the aspirated shield. The temperature error of the naturally ventilated shield itself is not taken into account. However, at wind speeds above 4 m/s, where the FLUENT simulations were compared to field data, the temperature error of naturally ventilated shields is thought to range from 0.01 to 0.1 °C [4]. Thus, a variation of 0.02 °C in the FLUENT model from simulation to simulation falls within an acceptable range when compared to the variation of determining temperature error experimentally in the field.

4. Artificial neural network

4.1. Introduction

Artificial neural networks are massively parallel, highly interconnected systems of computational nodes or neurons. A typical ANN structure consists of an input layer into which the independent variables in a specified problem are fed in, the output layer that produces the dependent variables and one or several hidden layers. The hidden layers link the input and output layers together and allow for complex, nonlinear interactions between the inputs to produce the appropriate outputs. Computations are performed in the hidden layers and the output layer, but not in the input layer.

An ANN is said to be "trained" if it "learns" the input–output behavior. To train an ANN, a set of input–output data are required that should be representative of the process. Different strategies are used to generate such data, see [12]. One useful strategy is to conduct carefully designed numerical experiments over the input domain to capture the general behavior of the process over the whole range of the input variables. Several algorithms are available to train an ANN. Marwah et al. [13] proposed an integrated approach to the model development which has been shown to be very effective and economical for different applications, see [12]. Following this methodology, the exemplars are divided into training data, testing data and validation data in a preset ratio (1/2, 1/4, 1/4 are typical values). The model development begins with a simple neural network architecture. This typically consists of one hidden layer with one neuron or with a number of neurons equal to half the sum of inputs and outputs. The latter rule is based on the first author's experience and is purely empirical. The training process starts with feeding training input data to the ANN, selecting a randomized set of weights and calculating the outputs by running the inputs through the network. The errors between the predicted output and the

actual values of the output are calculated. The weights are then updated to minimize the error by following the back propagation technique [13–15]. The process is repeated until the error is below a specified value. If a prescribed value of the accuracy is not achieved, another neuron is added. This process continues until a specified value of correlation coefficient (0.8) for the training data is reached. At this point, the ANN's performance is calculated on the testing data and the iterative process discussed earlier is followed until the desired accuracy measured by R^2 or ε_{REL} or ε_{MSE}, is achieved on the testing data. Following this, the model's performance is checked on the validation data set aside. If necessary, the ANN is retrained to achieve the desired accuracy on the validation data.

The three measures used to gauge performance of the CU-ANN mentioned above, ε_{REL}, ε_{MSE}, R^2 are defined as follows:

$$\varepsilon_{MSE} = \frac{1}{N}\sum_{i=1}^{N}(\hat{Y}_i - Y_i)^2$$

$$\varepsilon_{REL} = \frac{1}{N}\sum_{i=1}^{N}\left|\frac{\hat{Y}_i - Y_i}{Y_i}\right|$$

$$R^2 = 1 - \frac{\sum_{i=1}^{N}(\hat{Y}_i - Y_i)^2}{\sum_{i=1}^{N}(Y_i - \overline{Y})^2}$$

where N is the total number of data points, $\hat{Y}_i$ is the predicted output, Y_i is the actual output, and $\overline{Y}$ is the actual output mean. For the relative merits of these measures, see [13].

An attractive attribute of ANN models is their fast speed of computation. Once an ANN model has been trained, tested and validated, it can provide almost real-time parametric and sensitivity analysis. The typical time taken for an ANN model to execute one run is generally several orders of magnitude smaller than that required for running a CFD model [8].

4.2. Model development for MARS

In order to develop an ANN model for the shields, 72 FLUENT simulation runs described earlier in Section 3.3 were used as input file to the neural network. The input variables were inlet section configuration, length of shield/recessed length and wind speed. The output variable was the temperature error as measured by the difference between the sensor surface and the ambient temperatures.

For the verification data, a new set of input data that was not earlier used to train the network was generated. To this end, some of the above shield geometries were run with wind speeds of 2, 4, 6, and 8 m/s. In addition, a new bell-shaped inlet with a radius of curvature of 0.63 cm was created and run for wind speeds of 2, 4, 6, and 8 m/s to see how well the ANN could predict temperature errors for a new geometry.

Following the methodology briefly described in Section 4.1, an optimum network architecture was selected to develop the most accurate ANN model relating the inputs to the output. The optimum neural network structure was found to be 3–10–1 (three inputs, 10 neurons in the hidden layer, and 1 output neuron corresponding to temperature error). The optimum learning parameters of the neural network were a learning rate of 0.1 and a momentum of 0.9. The optimum number of epochs, or iterations for the model was 30,128. For this ANN model structure, the $\overline{\varepsilon}_{MSE}$ for training and testing were found to be 1.59E−04 and 6.67E−4, respectively. The $R^2_{training}$ and $R^2_{testing}$ were found to be 99% and 95.5%, respectively.

4.3. MARS model verification

To verify the validity of the ANN MARS model, the model was run on the verification runs described above in Section 4.2. The comparison showed an excellent agreement between the neural network and the FLUENT output for these verification trials. The mean squared error and relative error for these verification trials, as well as the FLUENT target values and ANN model predicted output for a few of the cases are shown in Table 5 and Fig. 6, respectively. The relative error (RE) of the verification trials is 6.04%. This value and the value of the mean squared error (MSE) of the the verification trials are within an acceptable range.

4.4. Sensitivity analysis

The MARS ANN model was used to perform a sensitivity analysis of shield performance with respect to the design variables. To this end, two of the three design variables were held constant while the third was allowed to vary slightly. The resulting changes in temperature error were recorded. The partial derivatives of temperature error were then obtained with respect to shield length, inlet radius of curvature, and wind speed for all FLUENT simulations, as follows:

$$\frac{(T_{L+\Delta L} - T_L)_{R,W}}{\Delta L} = \frac{\partial T}{\partial L} \tag{4}$$

$$\frac{(T_{R+\Delta R} - T_R)_{L,W}}{\Delta R} = \frac{\partial T}{\partial R} \tag{5}$$

$$\frac{(T_{W+\Delta W} - T_W)_{R,L}}{\Delta W} = \frac{\partial T}{\partial W} \tag{6}$$

where L is the shield length, R is the inlet radius of curvature, and W is the wind speed. These equations were used to generate three input files used in the ANN to perform the sensitivity analysis. The value of Δ used was 0.1% of the input value.

Table 5
Verification results

Validation MSE	4.248E−04
Validation RE (%)	6.04
Long shield MSE	2.543E−04
Long shield RE (%)	3.49
Medium shield MSE	2.430E−04
Medium shield RE (%)	5.05
Short shield MSE	7.773E−04
Short shield RE (%)	9.60

Several conclusions could be drawn from the results of the sensitivity analysis. First, the partial derivatives with respect to shield length show that the medium length shield is least sensitive to changes in shield length and the short shield is most sensitive to changes in length. Each shield's sensitivity to length increases with increasing wind speed and the sensitivity to length decreases with increasing inlet radius of curvature. Another interesting note about the partial derivatives with respect to length is that they are all positive for the long shield, indicating that longer shields yield higher temperature errors. For the short shield, all the partial derivatives are negative, indicating that temperature error is reduced by lengthening the shield. For the medium length shield, the partial derivatives are also negative, indicating that lengthening the shield slightly will yield even lower temperature errors.

For the partial derivatives with respect to inlet radius of curvature, the long shield is the most sensitive to inlet geometry. The medium length and short shields show roughly the same sensitivity to inlet geometry and are much less sensitive than the long shield. The overall sensitivity to inlet design decreases with increasing bell radius of curvature. In general, all shield lengths are more sensitive to inlet geometry at higher wind speeds, regardless bell radius of curvature.

The sensitivity of each shield design to wind speed shows that all shield lengths are less sensitive to wind for the larger inlets. Also, each shield length and inlet design is more sensitive to wind at the higher wind speeds in the 5–7 m/s range. Furthermore, the short and medium length shields are much less sensitive to wind speed than the long shield.

4.5. Design optimization

The MARS ANN model was also used in conjunction with a steepest descent optimization algorithm to help optimize the design. The goal here is to determine the shield length and inlet radius of curvature within the above input variable range that results in minimum temperature error for all wind speeds. Several initial guesses were used to ensure that the steepest descent algorithm did not converge to a local minimum.

The steepest descent optimization shows that the optimum outer shield length is 14.19 cm. This shield length results in the base of the temperature probe being recessed 6.06 cm from the inlet of the inner shield. This shield length is slightly longer than the medium length shield. The optimum inlet radius of curvature is 1.905 cm, corresponding to the largest bell-shaped inlet studied. This shield length was simulated in FLUENT with the large bell inlet. Runs were made for several wind speeds to confirm the network prediction. The resulting temperature errors for this geometry can be seen in Table 6. These temperature errors are indeed lower than the temperature errors for the medium length shield. The network prediction and the FLUENT experiments match very well.

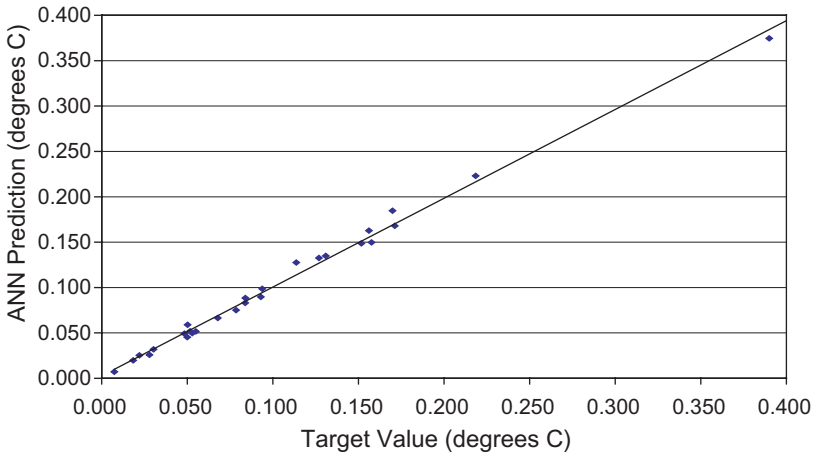

Fig. 6. Comparison between target and predicted output.

Table 6
Optimum shield geometry and confirmation results

Optimum settings	Wind speed (m/s)	Temperature error (°C) network predicted	Temperature error (°C) FLUENT results
Outer shield length 14.19 cm	0.1	0.019	0.023
	1	0.008	0.006
Inlet radius of curvature 1.91 cm	3	0.002	0.005
	5	0.042	0.046
	7	0.049	0.050
	9	0.041	0.048

One question that naturally arises is why the ANN is trained on the CFD results rather than directly on experimental data. One major reason for this is a lack of experimental data from the field for this specific MARS design. The only experimental data existing that can be interpreted in terms of temperature error are for the straight inlet, long shield length design from the OASIS98 field experiments. Other field experiments exist in which air temperature was recorded by the MARS with different inlet designs. However, there are no reference measurements in order to obtain temperature error values. CFD results used as input to the ANN, as long as the CFD results model the observed physics, allow more variables to be studied in less time and for lower cost since CFD model creation and simulation takes significantly less time than conducting a similar amount of field experiments. Also, it is cheaper than having numerous prototype shields built. With a combined CFD/ANN model, a more detailed analysis can be carried out in less time, thus allowing for more variables and a wider range of the variables to be studied.

5. Summary

In this investigation, we have combined a CFD model with a neural network model to predict errors in surface air temperature measurements for several mechanically aspirated radiation shield designs. The CFD model was developed to relate temperature errors to two geometric design variables and one environmental variable. The two geometry variables are the length of the vertical concentric shields (sensor placement) and the inlet radius of curvature. These variations were studied along with various ambient wind conditions. The temperature of the sensor surface minus the ambient air temperature was reported as the temperature error of the shield.

The simulations show that for the longer shield, the temperature error is a function of aspiration rate through the shield and flaring the inlet to allow for larger aspiration rates at high wind speeds can increase performance. These results are consistent with data from past field experiments and wind tunnel tests. As the shield length decreases, the errors become both a function of the convective and long wave radiative heat transfer processes. The sensitivity analysis suggests and the steepest descent optimization confirms that an optimum shield length exists that balances these two effects and minimizes temperature error. It shows that the optimum shield length is between the long and medium length shield, but very close to the medium length shield. Regardless of shield length, flared inlets improve convective cooling and the largest flare radius showed the most improvement in shield performance.

The resulting ANN model trained with the FLUENT data has a simple structure and yields good predictive capabilities. The predictive capability of the artificial neural network is encouraging. Additionally, the use of the neural network model in conjunction with the CFD model is preferred to performing a full analysis with just the CFD model. The speed and accuracy of the neural network allows fewer CFD tests to be carried out. Further, the ANN model serves as an excellent tool for achieving an optimum MARS design without extensive numerical simulations.

Acknowledgement

The first author gratefully acknowledges Chetan Malhotra's and Krishna Ramadurai's help in preparing the final version of the manuscript.

References

[1] F.V. Brock, P.K. Govind, Portable automated mesonet in operation, J. Appl. Meteorol. 16 (3) (1977) 299–310.
[2] F.V. Brock, G.H. Saum, S.R. Semmer, Portable automated mesonet II, J. Atmos. Oceanic Technol. 3 (4) (1986) 573–582.
[3] F.V. Brock, K.C. Crawford, R.L. Elliott, G.W. Cuperus, S.J. Stadler, H.L. Johnson, M.D. Eilts, The Oklahoma mesonet: a technical overview, J. Atmos. Oceanic Technol. 12 (1) (1995) 5–19.
[4] S.J. Richardson, F.V. Brock, S.R. Semmer, C. Jirak, Minimizing errors associated with multiplate radiation shields, J. Atmos. Oceanic Technol. 16 (11) (1999) 1862–1872.
[5] B.D. Tanner, E. Swiatek, C. Maughan, Field comparisons of naturally ventilated and aspirated radiation shields for weather station air temperature measurements, in: 22nd Conference on Agricultural and Forest Meteorology, Atlanta, Georgia, January 29–February 1, 1966, pp. 227–230, in preprints.
[6] G.C. Gill, Development of a small radiation shield for air temperature measurements on drifting buoys, NOAA Data Buoy Office Contract 01-7-038-827 (11), 1979. Available from: NOAA Data Buoy Office, Bay St. Louis, MS 39520.

[7] R.L. Mahajan, X.A. Wang, Neural network models for thermally based microelectronic manufacturing processes, J. Electrochem. Soc. 140 (8) (1993) 2287–2293.
[8] A.S. Kelkar, R.L. Mahajan, R.L. Sani, Real-time physiconeural solutions for MOCVD, J. Heat Transfer—Trans. ASME 118 (4) (1996) 814–821.
[9] V.V. Calmidi, R.L. Mahajan, Optimization for thermal and electrical performance for a flip-chip package using physical–neural network modeling, IEEE Trans. Comp. Packag. Manuf. Technol. C 21 (2) (1998) 111–117.
[10] M. Fuchs, C.B. Tanner, Radiation shields for air temperature thermometers, J. Appl. Meteorol. 4 (4) (1965) 544–546.
[11] F.P. Incropera, D.P. DeWitt, Fundamentals of Heat and Mass Transfer, third ed., John Wiley, New York, 1990.
[12] R.L. Mahajan, Neural nets for modeling, optimization and control in semiconductor manufacturing, Proc. SPIE 3812 (1999) 176–187.
[13] M. Marwah, Y. Li, R.L. Mahajan, Integrated neural network modeling for electronic manufacturing, J. Electron. Manuf. 6 (2) (1996) 79–91.
[14] M. Smith, Neural Network for Statistical Modeling, Van Nostrand Reinhold, New York, NY, 1989.
[15] P.J. Werbos, Beyond regression: new tools for prediction and analysis in the behavioral sciences, Ph.D. thesis, Harvard University, Boston, MA, 1974.